140 (2022) 213057

Contents lists available at ScienceDirect

Biomaterials Advances

journal homepage: www.journals.elsevier.com/materials-science-and-engineering-c

Enhancement of photoactivity and cellular uptake of $(Bu_4N)_2[Mo_6I_8(CH_3COO)_6]$ complex by loading on porous MCM-41 support. Photodynamic studies as an anticancer agent

Cristina de la Torre [a,b], Raquel Gavara [c], Alba García-Fernández [a,b,e], Maxim Mikhaylov [d], Maxim N. Sokolov [d], Juan F. Miravet [c], Félix Sancenón [a,b,e,f], Ramón Martínez-Máñez [a,b,e,f,**], Francisco Galindo [c,*]

[a] Instituto Interuniversitario de Investigación de Reconocimiento Molecular y Desarrollo Tecnológico (IDM), Unidad Mixta Universitat Politècnica de València - Universidad de Valencia, Departamento de Química Universitat Politècnica de València, Camino de Vera s/n, 46022 Valencia, Spain
[b] CIBER de Bioingeniería, Biomateriales y Nanomedicina, Instituto de Salud Carlos III, Spain
[c] Departamento de Química Inórganica y Orgánica, Universitat Jaume I, Av. Sos Baynat s/n, 12071 Castellón, Spain
[d] Nikolaev Institute of Inorganic Chemistry, Siberian Branch of the Russian Academy of Sciences, 3 Acad. Lavrentiev Prosp., 630090 Novosibirsk, Russia
[e] Unidad Mixta UPV-CIPF de Investigación en Mecanismos de Enfermedades y Nanomedicina, Universitat Politècnica de València, Centro de Investigación Príncipe Felipe, Valencia, Spain
[f] Unidad Mixta de Investigación en Nanomedicina y Sensores, Universitat Politècnica de València, IIS La Fe, Valencia, Spain

ARTICLE INFO

Keywords:
Hexamolybdenum cluster
Mesoporous silica nanoparticles
Photodynamic therapy
Singlet oxygen
HeLa cells
Melanoma cells

ABSTRACT

The incorporation by ionic assembly of the hexanuclear molybdenum cluster $(Bu_4N)_2[Mo_6I_8(CH_3CO_2)_6]$ (**1**) in amino-decorated mesoporous silica nanoparticles **MCM-41**, has yielded the new molybdenum-based hybrid photosensitizer **1@MCM-41**. The new photoactive material presents a high porosity, due to the intrinsic high specific surface area of **MCM-41** nanoparticles (989 $m^2\ g^{-1}$) which is responsible for the good dispersion of the hexamolybdenum clusters on the nanoparticles surface, as observed by STEM analysis. The hybrid photosensitizer can generate efficiently singlet oxygen, which was demonstrated by using the benchmark photooxygenation reaction of 9,10-anthracenediyl-bis(methylene)dimalonic acid (ABDA) in water. The photodynamic therapy activity has been tested using LED light as an irradiation source ($\lambda_{irr} \sim$ 400–700 nm; 15.6 mW/cm^2). The results show a good activity of the hybrid photosensitizer against human cervical cancer (HeLa) cells, reducing up to 70 % their viability after 20 min of irradiation, whereas low cytotoxicity is detected in the darkness. The main finding of this research is that the incorporation of molybdenum complexes at porous **MCM-41** supports enhances their photoactivity and improves cellular uptake, compared to free clusters.

1. Introduction

The photosensitized generation of reactive oxygen species (ROS) is used in a wide range of applications, from photocatalysis [1–4] to antimicrobial photodynamic inactivation (aPDI) [5–9] and photodynamic therapy of cancer (PDT) [10–14]. One of the most frequently used ROS species in the biomedical context is singlet oxygen O_2 ($^1\Delta g$). This highly reactive species is formed when the triplet excited state of certain photosensitizer molecules transfers its excess energy to molecular oxygen [15–18]. Molybdenum clusters with the formula $[Mo_6X_8L_6]^{2-}$ (where X = Cl, Br, I; and L is a ligand) are well-known singlet oxygen photosensitizers [19–23]. In this kind of complex, six Mo(II) atoms form an octahedral cluster and are surrounded and strongly bound to eight bridging atoms and six labile apical ligands. When irradiated with near UV or visible light below 450 nm, these complexes exhibit phosphorescence due to an efficient intersystem crossing to form triplet states that relax to the ground state emitting in the red-NIR wavelengths range. This phosphorescence is deactivated in the presence of molecular

* Correspondence to: F. Galindo, Departamento de Química Inórganica y Orgánica, Universitat Jaume I, Av. Sos Baynat s/n, 12071 Castellón, Spain
** Correspondence to: R. Martínez-Máñez, Instituto Interuniversitario de Investigación de Reconocimiento Molecular y Desarrollo Tecnológico (IDM), Unidad Mixta Universitat Politècnica de València - Universidad de Valencia, Departamento de Química Universitat Politècnica de València, Camino de Vera s/n, 46022 Valencia, Spain.
E-mail addresses: rmaez@qim.upv.es (R. Martínez-Máñez), francisco.galindo@uji.es (F. Galindo).

https://doi.org/10.1016/j.bioadv.2022.213057
Received 9 March 2022; Received in revised form 26 July 2022; Accepted 27 July 2022
Available online 2 August 2022

oxygen to produce singlet oxygen in high yields. The photophysical properties exhibited by these complexes have allowed their use in applications such as heat insulation materials [24], sensing of oxygen [25,26], development of luminescent materials [27–32], electro-optic devices [33], bioimaging [34,35], photocatalysis [9,36–40], aPDI [8,9,41,42] and PDT [41,43–49], among others. Hexanuclear molybdenum clusters have been proved to be superior to other photosensitizers described in the literature in terms of resistance to photobleaching [9] and luminescence lifetimes [23,34] which opens the door to theranostic applications. Additionally, in recent times they have been described also as efficient agents for X-ray induced therapies [45].

Despite the high performance of hexamolybdenum clusters as singlet oxygen photosensitizers, the main drawback concerning the application of these compounds in PDT is their low stability in water. In this solvent, the clusters have a high tendency to hydrolyze even at neutral pH values, by replacement of the labile ligands with water and hydroxy groups. The hydrolyzed complexes tend to aggregate and precipitate, losing their photoactivity in solution [36,50–53]. Moreover, these clusters are generally anionic in an aqueous environment, making their internalization into cells through the cell membrane very difficult. An important strategy to avoid or minimize the hydrolysis facilitating at the same time the cellular uptake is the use of nanocarriers. Thus, the encapsulation of hexamolybdenum clusters in polystyrene nanoparticles [47], PLGA nanoparticles [44,54], a chromium-terephthalate metal-organic framework nanocarrier [46] and non-porous silica nanoparticles [43,48] for their use in PDT applications have been reported.

Important nanocarriers that have been up to date unexplored in PDT applications with hexamolybdenum clusters are mesoporous silica nanoparticles (MSNs) which present multiple advantages for the encapsulation of bioactive drugs and photosensitizers for PDT [55,56], namely, high specific surface area, large pore volumes, tunable pore size, highly homogeneous porosity, easy functionalization, high loading capacities, good chemical and biological stability, biocompatibility and optical transparency. Cellular uptake can be easily modulated by using appropriate functional groups and even biomolecules anchored on the silica surface [57–61]. Moreover, the size of nanoparticles of the order of 100 nm or fewer results very convenient to facilitate the cellular uptake by endocytosis [62,63]. Photosensitizers such as porphyrins [64–67], phthalocyanines [68,69], xanthenic [70] and squaraine [71] based dyes have been incorporated into mesoporous silica nanoparticles to develop PDT anticancer materials.

Taking all these into consideration, in this work, we aimed at a new photosensitizer material through the encapsulation in **MCM-41** mesoporous silica nanoparticles of the hexamolybdenum cluster $(Bu_4N)_2[Mo_6I_8(CH_3CO_2)_6]$ (**1**) [72] with acetate apical ligands, that has shown a good photoactivity in different applications [8,9,43,73]. Cluster **1** is adsorbed onto mesoporous silica nanoparticles functionalized with ammonium groups (**APTES@MCM-41**), which effectively loads the cluster anions by electrostatic interactions (Fig. 1). This approach has been used in the past for loading hexamolybdenum clusters in different solid matrices [8,9,29,43,74,75] but, to the best of our knowledge, this is the first time that a matrix based on mesoporous silica nanoparticles is used. Due to the large porosity and high surface area of **MCM-41**, cluster **1** can be efficiently loaded and dispersed on the nanoparticles, while remaining well protected against hydrolysis. It is expected that the high dispersion of the cluster on the matrix surface will favour the generation of singlet oxygen upon irradiation. To check this hypothesis, the PDT efficiency of the new photosensitizer material versus the free cluster was tested against human cervical cancer (HeLa) and melanoma (SK-Mel-103) cells.

2. Materials and methods

2.1. Materials

The chemical reagents tetraethylorthosilicate (TEOS), *n*-cetyltrimethylammonium bromide (CTABr), sodium hydroxide (NaOH), (3-aminopropyl) triethoxysilane (APTES, 99 %), Pluronic® F-127, 9,10-anthracenediyl-bis(methylene)dimalonic acid (ABDA, ≥90 %), as well as the reagents to prepare the phosphate-buffered saline (PBS) solution namely, RPMI 1460 media (R8758), lipopolysaccharide (LPS) from *Escherichia coli* O111:B4 (L2630-100MG), nigericin (NG) (N7143-5MG), Crystal Violet, Cell Proliferation Reagent WST-1, NaCl (≥99 %), KCl (≥99.0 %), Na_2HPO_4 (≥99.0 %) and KH_2PO_4 (≥99.5 %) were supplied

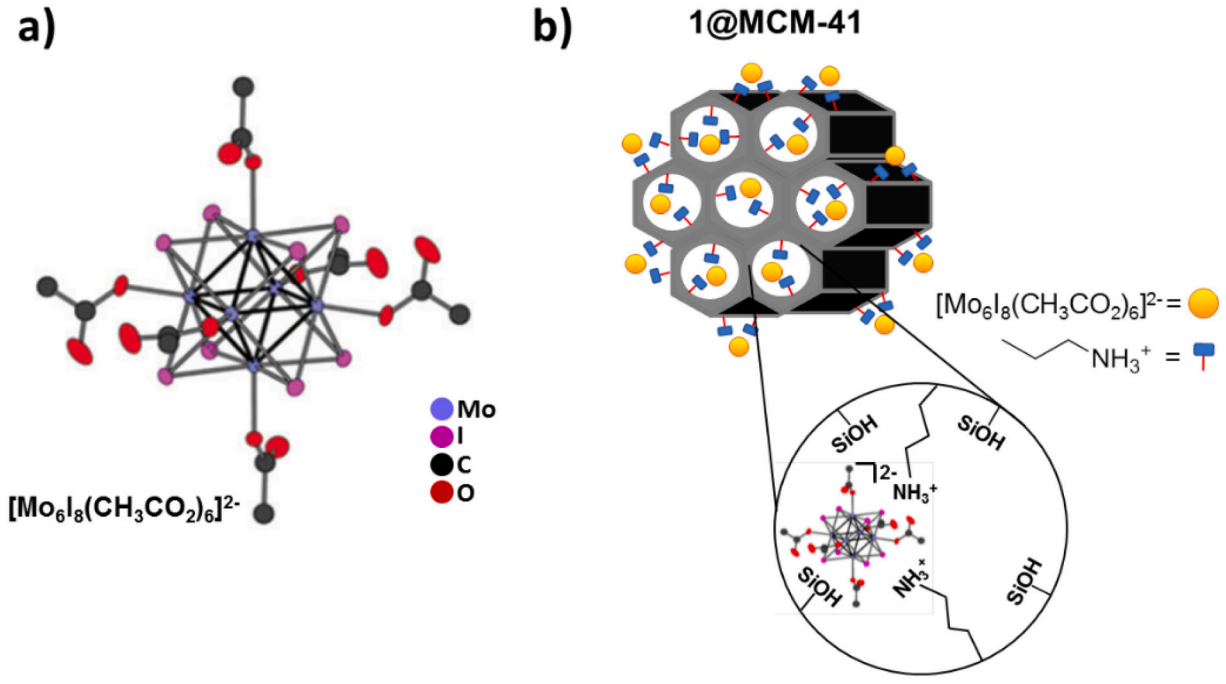

Fig. 1. a) Anionic form of cluster **1**. b) Encapsulation of cluster **1** in amino decorated mesoporous silica nanoparticles gives rise to the hybrid photosensitizer **1@MCM-41**.

by Sigma-Aldrich, 3-(4,5-Dimethyl-2-thiazolyl)-2,5-diphenyl-2H-tetrazolium bromide (MTT) was acquired from Serva. LDH activity assay was purchased from Promega (G7891). Human IL-1β ELISA Set II was obtained from BD Biosciences (557953). Penicillin/streptomycin, Dulbecco's modified Eagle's medium (DMEM), minimum essential medium (MEM), fetal bovine serum (FBS) and Dulbecco's phosphate-buffered saline (DPBS), were supplied by Biowest. Solvents THF, CH_2Cl_2 and CH_3CN were acquired from Scharlab, S.L. Distilled water was used to prepare the aqueous solutions. Hexanuclear cluster $(Bu_4N)_2[Mo_6I_8(CH_3CO_2)_6]$ (**1**) was synthesized according to the procedure reported in the literature [72].

2.2. Cultivation of cell lines

Cell lines were acquired from the American Type Culture Collection (ATCC). HeLa cell line was cultured in DMEM medium containing 10 % fetal bovine serum, 1 % penicillin/streptomycin and 2 mM L-glutamine. SK-Mel-103 cell line was cultured in Minimum Essential Medium supplemented with 10 % fetal bovine serum. THP-1 cells were cultured in RPMI 1640 media with 10 % fetal bovine serum. The cell lines were kept in a monolayer culture at 37 °C in a humidified atmosphere containing 5 % CO_2.

2.3. Instrumentation

Powder X-ray diffraction (PXRD) analysis of the materials was performed in a Philips D8 Advance diffractometer using CuKα radiation. Transmission Electron Microscopy (TEM) images were acquired using a 100 kV Philips CM10 microscope. Scanning Transmission Electron Microscopy (STEM) and Energy Dispersive X-Ray Spectroscopy (EDS) analysis were recorded with a JEOL JEM 2100F (200 Kv). Thermogravimetric measurements were performed on a TGA/SDTA 851e Mettler Toledo balance using an oxidant atmosphere (air, 80 mL/min). The heating program consisted of a heating ramp (10 °C min^{-1}) from 120 °C to 1000 °C and an isothermal heating step at this temperature for 30 min. Inductively coupled plasma mass spectrometry (ICP-MS) was performed on a spectrometer Agilent 7900 in H2 mode, with germanium as an internal reference. N_2 adsorption-desorption isotherms were acquired using a Micromeritics ASAP2010 automated sorption analyser. Confocal laser scanning microscopy (CLSM) images were recorded on an inverted confocal microscope Leica TCS SPE using an ACS APO 40X/1.15 Oil CS objective. Dynamic light scattering (DLS) and zeta potential measurements were performed in a Zetasizer Nano ZS (Malvern Instruments). Solutions were filtered before the measurements using a 0.45 μm Millipore nylon membrane filter and every analysis was carried out three times. All samples with nanoparticles were sonicated for 30 min before measurements. The pH values of the solutions were measured with a CRISON pH meter GLP 21. The UV–vis absorption measurements were made using an Agilent Cary 60 UV–Vis Spectrometer. The steady-state emission spectroscopy was performed in an Agilent Cary Eclipse spectrofluorometer. The excitation wavelength was set at 420 nm. The luminescence at 1270 nm corresponding to $O_2(^1\Delta_g)$, was recorded using a modular Horiba FluoroLog-3 spectrofluorometer. The quantum yields of singlet oxygen generation, Φ_Δ, were measured in oxygen-saturated acetonitrile using anthracene as a standard with known quantum yield ($\Phi_\Delta = 0.69 \pm 0.02$) [76]. All the solutions presented the same absorbance at the wavelength of excitation (308 nm).

2.4. Synthesis of mesoporous silica nanoparticles (*MCM-41*)

An aqueous solution (480 mL) of the surfactant *n*-cetyltrimethylammonium bromide (CTABr, 1.00 g, 2.74 mmol) was prepared and basified with 3.5 mL of NaOH 2 M solution. Then, TEOS (5 mL, 2.57 $\times 10^{-2}$ mol) was slowly added to this solution at a temperature of 80 °C. After 2 h of stirring, a white precipitate was obtained. The solid was separated by centrifugation, washed with distilled water and dried at a temperature of 60 °C. The final mesoporous material (**MCM-41**) was obtained by calcination of the solid at 550 °C for 5 h in the presence of an oxidizing atmosphere, to remove the template phase.

2.5. Synthesis of *APTES@MCM-41*

(3-aminopropyl) triethoxysilane (240 mL, 1 mmol) was added dropwise to a suspension of **MCM-41** (200 mg) in acetonitrile (15 mL) at room temperature. After 12 h of stirring, the resulting solid was separated by filtration, washed with acetonitrile and dried under vacuum.

2.6. Synthesis of the hybrid photosensitizer *1@MCM-41*

The incorporation of the hexamolybdenum cluster into the functionalized **MCM-41** nanoparticles was accomplished by following a procedure based on that reported in the literature for non-porous silica nanoparticles [43]. Basically, an aqueous solution of cluster **1** (0.035 M) containing Pluronic® F-127 (0.3 mM) was mixed with an aqueous suspension of **APTES@MCM-41** (0.5 g L^{-1}). The mixture was shaken for 10 min and then sonicated for 15 min. **1@MCM-41** nanoparticles were separated by centrifugation at 9000 rpm, washed with water and dried under vacuum.

2.7. Benchmark photooxidation reaction for measuring $^1O_2$ production

Neutral aqueous solutions of ABDA (3.3×10^{-5} M, PBS 10 mM) were mixed with the corresponding heterogeneous (**1@MCM-41**, 0.1 mg mL^{-1}) or homogeneous (**1**, 2.9×10^{-5} M) photosensitizers in quartz cuvettes. Control experiments with blank **MCM-41** and in the absence of any photosensitizer were also performed. The mixtures were stirred continuously and irradiated with the light provided by two LED lamps (Lexman; $\lambda_{irr} \sim$ 400–700 nm; power: 11 W each; irradiance: 15.6 mW/cm^2) separated from the cuvette by a distance of 3 cm. The photooxygenation reaction of ABDA was followed by monitoring the decrease of the absorption band at 380 nm. The photooxidation rates were calculated considering a pseudo-first order kinetics model.

2.8. Crystal violet staining

HeLa and SK-Mel-103 cells were seeded in a 24-well plate at a density of 35,000 cells/well. The complex 1 and the 1@MCM compounds were added the following day at 200 μg/mL for 24 h. Then, the cells were washed with PBS and fixed with paraformaldehyde 4 % (15 min, RT). After incubation time, the cells were washed, and the crystal violet solution (0.05 %) was added for 45 min. Finally, the cells were washed with water to discard the excess the dye and dried at RT before visualization.

2.9. Immune activation assays

THP-1 cells were seeded in a 6 well-plate at 800,000 cells/mL in RPMI 1 % FBS and incubated for 24 h. Next, the cells were treated for 24 h with complex 1 and 1@MCM-41 at 14.3 μM and 200 μg/mL, respectively. After the incubation time, as a positive control for immune activation, the untreated cells (without the compounds) were stimulated with lipopolysaccharide (LPS) from *E. coli* (100 ng/mL) for 3 h and nigericin (NG) at 20 μM during the last 30 min of incubation to activate the NLPR3 inflammasome and thus the inflammatory response. The inflammatory activity was evaluated by measuring the secretion of inflammatory cytokines, such as interleukin-1βeta (IL-1β) by ELISA kit following supplier's instructions (Human IL-1β ELISA Set II, ref. 557953). Besides, lactate dehydrogenase (LDH) activity, as marker of the inflammatory mode of regulated cell death, was measured through the LDH Assay Kit II following manufacturer instructions.

2.10. Confocal laser scanning microscopy (CLSM)

HeLa cells were seeded on microscope slides (1.5×10^5 cells per slide) and incubated for 18 h at 37 °C under an atmosphere containing 5 % CO_2. After that, the medium was replaced with a fresh medium containing **1@MCM-41** (50 μg/mL) or cluster **1** (3.5 μM) and incubated for 2 h. Controls were also performed, incubating cells in the absence both of silica nanoparticles and cluster **1**. After the incubation, the cells were doubly washed with DPBS, fixed in 4 % paraformaldehyde, and washed again with DPBS two times. Cells were visualized on an inverted confocal microscope Leica TCS SPE. The recorded pictures were analysed with Image J software. The experiments were performed in triplicate on separate days.

2.11. Cytotoxicity of the nanoparticles

In a first step, the possible toxicity of the nanoparticles was evaluated by cell viability assays at different concentrations. HeLa and SK-Mel-103 cells were seeded at 5000 cells/well in a p96 well-plate for 24 h. Then different concentrations of the complex 1 (0 to 30 μM) and **1@MCM-41** (0 to 500 μg/mL) were added. After 24 h, 10 μL of the Cell Proliferation Reagent WST-1 were added to each well and the plates incubated for 1 h. The absorbance was measured at 450 nm in a spectrophotometer Wallac 1420 Victor2 Microplate Reader (PerkinElmer).

On the other hand, 3-(4,5-Dimethyl-2-thiazolyl)-2,5-diphenyl-2H-tetrazolium bromide (MTT) assay was used to study the cytotoxic activity of the nanoparticles for PDT purposes. Cells were incubated at 37 °C in a humidified atmosphere containing 5 % CO_2. After trypsinisation, harvesting and counting, cells were seeded in 96-well plates at a density of 2.5×10^3 for HeLa cells/well or 5×10^3 for SK-Mel-103 cells/well. After 24 h, the medium was replaced with a cell culture medium containing 100 and 200 μg/mL of **MCM-41** or **APTES@MCM-41** nanoparticles and further incubated for 24 h. Then, the cells were washed two times with Dulbecco's phosphate-buffered saline (DPBS) and afterwards incubated for 45 min with a cell culture medium containing MTT (0.5 mg mL^{-1}). After removal of the medium, formazan crystals were solubilized in DMSO. Measurements of the absorbance at 565 nm were performed with a microplate reader and the cell viability was calculated using the formula $[A_{565}]_{MCM}$ / $[A_{565}]_{control}$ * 100, where $[A_{565}]_{MCM}$ corresponds to samples containing either **MCM-41** or **APTES@MCM-41** and $[A_{565}]_{control}$ is the value for a control cell culture non-treated with nanoparticles. All experiments were performed in triplicate, with three replicates per experiment.

2.12. Photodynamic treatment

Cells were seeded in 96-well plates in 200 μL of DMEM at a density of 2.5×10^3 cells/well for HeLa cells or 5×10^3 for SK-Mel-103 cells. After 24 h of incubation, the cell culture medium was replaced with a new one containing the corresponding nanoparticles (100 or 200 μg/mL) or cluster **1** (14.3 or 7.3 μM) and incubated for 6 h. Then, the cells were doubly washed with DPBS and supplemented with fresh medium. Irradiation was performed using light-emitting diodes (LED, 15.6 mW/cm^2) at 400–700 nm for 20 min, placing the samples at a distance of 3 cm to the LED source which resulted in a light dose of 19 J/cm^2. The viability of the irradiated cells was quantified by the MTT assay. The relative cell viability was calculated regarding control cell cultures non-treated with nanoparticles nor cluster **1** and non-irradiated, using the formula $[A_{565}]_x$ / $[A_{565}]_{control}$ * 100, where $[A_{565}]_x$ is the absorbance at 565 nm of the samples incubated with nanoparticles or cluster **1** which can be either irradiated or non-irradiated whereas $[A_{565}]_{control}$ is the absorbance at 565 nm of the control cells culture. Three independent experiments, counting three replicates each, were carried out.

3. Results and discussion

The nanosized hybrid material **1@MCM-41** was prepared by combining mesoporous silica **MCM-41** and the hexanuclear molybdenum complex **1**. **MCM-41** nanoparticles possess several characteristics such as inertness, high homogeneous porosity, high load capacity, and ease of surface functionalization which make them very attractive materials to develop new hybrid photosensitizers [58,59,69,77–79].

The hexanuclear cluster $(Bu_4N)_2[Mo_6I_8(CH_3CO_2)_6]$ (**1**) was synthesized following the procedure reported in the literature [72]. To encapsulate the cluster into the mesoporous silica, template-free nanoparticles (calcined **MCM-41**) were first functionalized with (3-aminopropyl)triethoxysilane (**APTES@MCM-41**) which provided positive charges on the surface of the nanoparticles by protonation of the amino groups in water [43].

The final ionic assembly between the amino-decorated silica nanoparticles and the $[Mo_6I_8(CH_3CO_2)_6]^{2-}$ cluster units to yield **1@MCM-41** (Scheme 1) was achieved by mixing a Pluronic® F-127 triblock copolymer based-solution of **1** with **APTES@MCM-41** nanoparticles, following a protocol similar to that reported by Elistratova et al. [43]. They demonstrated that the use of a poloxamer increases the solubility of the molybdenum cluster in an aqueous solution and improves the subsequent loading in non-porous silica. In the present work, we go a step forward using mesoporous silica **MCM-41** as the inorganic scaffold which due to its high specific surface area is expected to increase substantially the number of molybdenum photoreactive centres on the surface of the nanoparticles.

MCM-41, **APTES@MCM-41**, and **1@MCM-41** nanoparticles were thoroughly characterized using several analytical techniques. PXRD of the **MCM-41** nanoparticles before calcination showed four low-angle peaks, typical for the hexagonal-ordered pore array exhibited by this material, which corresponds to the (100), (110), (200) and (210) Bragg reflections. The diffractogram of **MCM-41** after calcination shows a shift of the (100) peak and a significant broadening of the (110) and (200) peaks. These changes can be attributed to further condensation of silanol groups during the calcination process. Importantly, the analysis confirms that the hexagonal porous array is preserved in the final hybrid material **1@MCM-41**, as confirmed by the persistence of the characteristic (100) reflection in the diffraction pattern (see Fig. S1 in Supplementary Material).

N_2 adsorption-desorption analysis was performed on **MCM-41** samples before and after calcination. The calcined NPs of **MCM-41** showed an adsorption step at an intermediate value of P/P_0 comprised between 0.1 and 0.3. The isotherm could be classified as type IV and is characteristic of mesoporous materials. The application of the BET model resulted in a value for the total specific surface area of 989 m^2 g^{-1}. The pore size distribution (PSD) of this sample was calculated by Barret-Joyner-Halenda (BJH) method, obtaining a value of pore diameter of 2.49 nm and pore volume of 0.86 cm^3 g^{-1}. In contrast, the N_2 adsorption-desorption isotherm of **MCM-41** before calcination was typical for mesoporous systems with mesopores filled with the CTABr template (Fig. 2).

Fig. 3 shows TEM (transmission electron microscopy) and STEM (scanning transmission electron microscopy) images of **APTES@MCM-41** (Fig. 3A) and final nanoparticles **1@MCM-41** (Fig. 3B). The micrographs allow observing the characteristic porosity associated with **MCM-41**, with a diameter of ca. 100 nm, in agreement with the size measured by DLS (Fig. S2). In the case of **1@MCM-41,** the black dots indicate the incorporated molybdenum clusters. The STEM analysis of **1@MCM-41** (Fig. 3C) shows a sharper contrast between the silica support and the metal cluster aggregates which appear as white dots. In fact, energy-dispersive X-ray spectroscopy (EDX, 20 kV) confirms unequivocally the presence of molybdenum and iodine heavy atoms in the white spots. This technique is very useful to prove the presence of hexamolybdenum clusters in inorganic supports and was used to analyse the presence of the clusters in ZnO nanocrystals [80] and non-porous silica

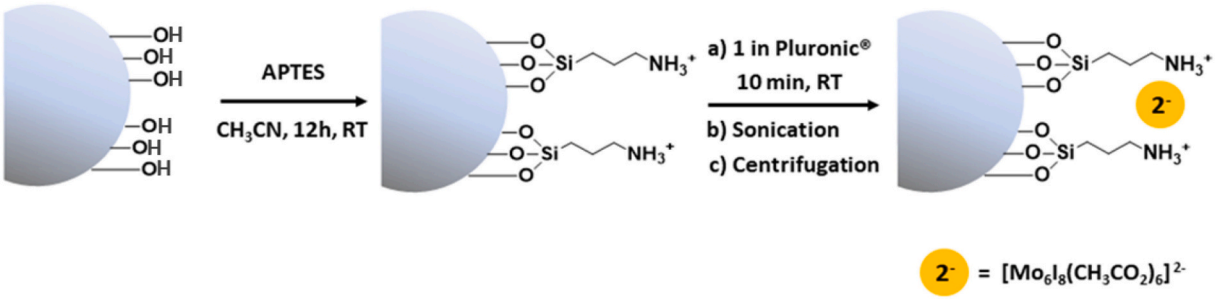

Scheme 1. Chemical reaction of calcined **MCM-41** with APTES and subsequent incorporation of **1** to obtain **1@MCM-41**.

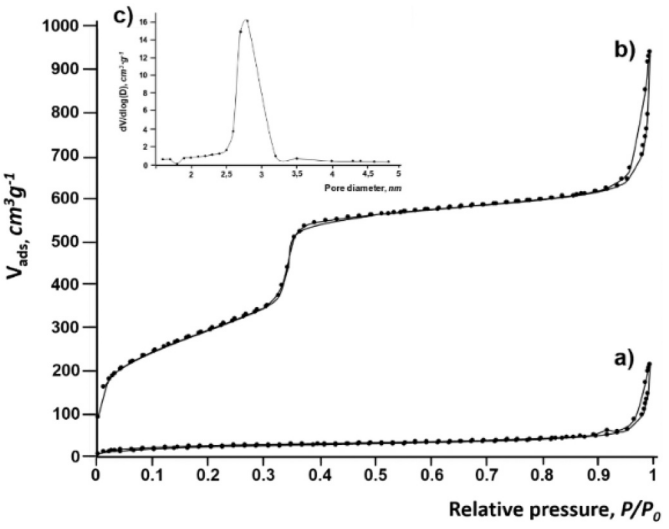

Fig. 2. Adsorption-desorption isotherms for (a) **MCM-41** nanoparticles before calcination and (b) **MCM-41** calcined after surfactant extraction; together with pore-size distribution (c).

nanoparticles obtained by water-in-oil microemulsions [31,81]. In our system, additional elemental mapping analysis of molybdenum and iodine indicates that both elements are distributed together in the nanoparticles, indicating good dispersion of the hexamolybdenum clusters in the mesoporous silica.

The efficiency of the assembly protocol was furthermore confirmed by ICP-MS, which allowed the quantification of Mo and Si contents. In addition, from thermogravimetric analyses, the APTES content was determined. The corresponding values are 1.09 mmol g^{-1} SiO_2 for APTES and 0.015 mmol g^{-1} SiO_2 for hexamolybdenum cluster **1**. Indirect observation of the incorporation of APTES and **1** into the silica nanoparticles is supplied from zeta potential measurements of the corresponding nanoparticles. The potential switched dramatically from −27 mV to +33 mV after the functionalization with APTES, due to the presence of protonated amino groups on the surface of the nanoparticles. Subsequent incorporation of the anionic $[Mo_6I_8(CH_3CO_2)_6]^{2-}$ units caused a reduction of the zeta potential to +4 mV. Moreover, after loading of **1**, the amino decorated silica nanoparticles acquired the characteristic yellow colour from the cluster. Additionally, visualization of the **1@MCM-41** colloidal suspension in neutral aqueous solution (PBS 10 mM) under UV light (365 nm), showed the typical red emission from the cluster (Fig. 4A) [72].

The emission spectra of **1** and **1@MCM-41** in aqueous media are shown in Fig. 4B. A redshift in the emission maximum from 661 to 716 nm was observed after loading the hexamolybdenum cluster in the mesoporous silica nanoparticles, together with a broadening of the emission band that is compatible with different microenvironments surrounding the cluster in the particles. Similar redshifts have been observed in analogous systems combining Mo_6 clusters and SiO_2 particles and can be attributed to the partial substitution of the apical acetate ligands by the siloxy and amino groups present in the nanoparticles [43], as well as hydroxy and water ligands [82,83]. The emission of both samples decreased remarkably after bubbling oxygen for 15 min, due to the more efficient energy transfer process from the photosensitizer to molecular oxygen and the subsequent formation of singlet oxygen (Fig. S3). The emission of **1@MCM-41** NPs was also recorded in the presence of organic solvents as shown in Fig. 4C. In this case, it is possible to see a slight red shift in the emission with the decrease of solvent polarity. On the other hand, **1@MCM-41** shows very weak emission as a powder, in the absence of any solvent (data not shown).

The generation of singlet oxygen by **1@MCM-41** in water was evaluated using a well-known benchmark reaction such as the reaction of 9,10-anthracenediyl-bis(methylene)dimalonic acid (ABDA) with $^1O_2$ to give the corresponding endoperoxide [84]. This reaction can be easily followed by UV–vis absorption spectroscopy. As a representative example, Fig. 5A shows the monitoring by UV–vis absorbance changes of the photooxygenation of ABDA (3.3×10^{-5} M) in PBS 10 mM (pH = 7) in the presence of 0.1 mg mL^{-1} of **1@MCM-41** nanoparticles. The decrease in the absorption maximum at 380 nm, due to the formation of the endoperoxide, was followed. The sample was initially stirred in the dark for 10 min and then irradiation was performed. The changes in the absorption after starting the irradiation are very clear in Fig. 5A, the sample is completely bleached after only 2 min of irradiation.

Determination of the pseudo-first order rate constant (k) is accomplished by following the absorption decrease at 380 nm as a function of the time of irradiation and the magnitude of the kinetic constant can be used as an estimation of the photoactivity of the material (Figs. 5B and S4). Analogous experiments were performed in the presence of **APTES@MCM-41** nanoparticles (0.1 mg mL^{-1}), free compound **1** (2.9×10^{-5} M) and in the absence of photosensitizer (self-oxidation of ABDA). Fig. 5B shows that **1@MCM-41** is the most active system while the blank **APTES@MCM-41** has very little effect when compared with the self-oxidation control. The rate constant calculated for **1@MCM-41** is >3.5 times higher than the value determined for compound **1** (0.548 vs. 0.151 min^{-1}).

This result is striking because the concentration of the Mo_6 cluster in the irradiated samples of **1@MCM-41** is >10 times lower than the concentration in the samples corresponding with the free cluster **1**. To be precise, the concentration of the Mo_6 in **1@MCM-41** used in the irradiations was 1.5×10^{-6} M, according to the ICP-MS analysis of the material. So, the differences in rate and concentration corroborate the hypothesis that the use of the highly porous support **MCM-41** improves the photooxygenation efficiency of the hexamolybdenum cluster due to the high dispersion of **1** on the surface of the material (as confirmed by STEM), preventing the inactivation of the photoactive centres.

Additionally, the measurement of the $O_2(^1\Delta_g)$ luminescence at 1270 nm (Fig. S5) allowed us to determine the quantum yield of singlet oxygen formation, ϕ_Δ, corresponding to cluster **1**, using the comparative method with anthracene as singlet-oxygen photosensitizer standard in oxygen-saturated acetonitrile [76]. The calculated value $\phi_\Delta = 0.86$, is

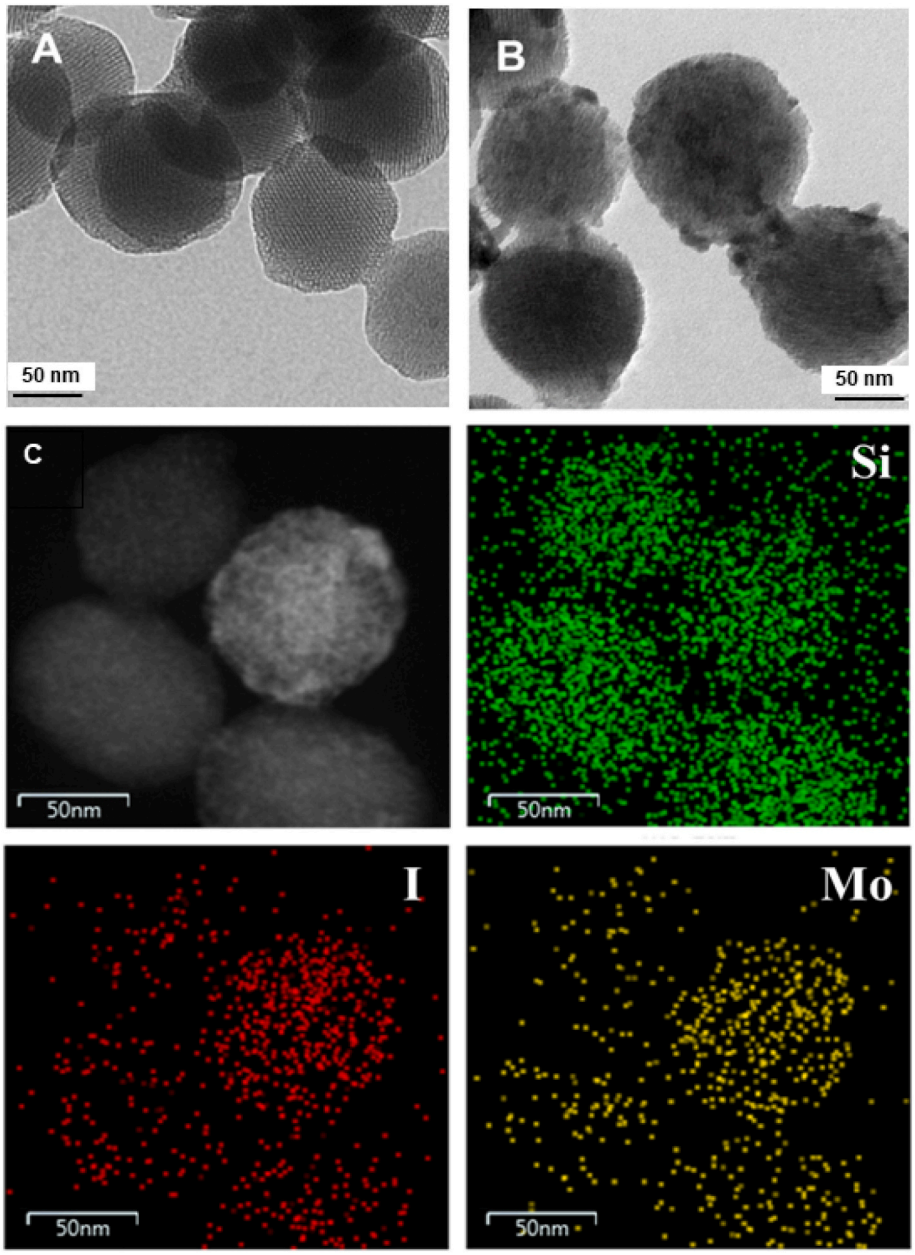

Fig. 3. TEM images of **APTES@MCM-41** NPs (A) and **1@MCM-41** NPs (B) and STEM micrograph of **1@MCM-41** NPs (C) with mapping of silicon (green), iodine (red) and molybdenum (yellow) via energy-dispersive X-ray spectroscopy. (For interpretation of the references to colour in this figure legend, the reader is referred to the web version of this article.)

identical to the reported one for the analogous compound $(nBu_4N)_2[Mo_6I_8(CF_3CO_2)_6]$ ($\phi_\Delta = 0.86$) [82]. Unfortunately, in the case of **1@MCM-41,** it was not possible to register the $O_2(^1\Delta_g)$ luminescence at 1270 nm because of the high light dispersion originated from the nanoparticle suspension.

An important factor to consider for the potential application of the photosensitizer nanoparticles is their stability in solution. In Fig. 6A the normalized emission of fresh **1@MCM-41** aqueous solution (0.1 mg mL^{-1}) is compared with that from the samples stored for 2 and 7 days respectively. A slight redshift of the emission with time is observed with stabilization occurring approximately after 2 days. This shift can be attributed to some aquation and hydrolysis. It is also worth noting that the intensity of emission does not show significant changes during the measured period. Analogous studies are displayed in Fig. 6B for solutions of the free compound **1** (2.9×10^{-5} M). In this case, the red shift in the emission due to hydrolysis and aquation is much more relevant and the emission maximum shifts about 30 nm after two days. These results indicate that free compound **1** is much more prone to react in water than that supported in **1@MCM-41** [43].

The activity of the fresh and aged samples (2 and 7 days) in the photooxygenation of ABDA was compared (Fig. 7). Free compound **1** shows very similar activity for the three samples, with a slight decrease after 7 days. In the case of **1@MCM-41,** an increase in the activity was observed after 2 days. The results are indicative of two facts: i) the system evolved from **1@MCM-41** does not precipitate significantly in the period evaluated and conditions used in this study (PBS 10 mM, pH = 7); ii) the photoactivity of the nanoparticles is maintained despite the ageing process. These results are in agreement with the behaviour of analogue compounds, where hydrolysis changes the luminescence of the complexes but does not reduce the ability to produce singlet oxygen, which can become even better in aged samples [41,52].

After the evaluation of the singlet oxygen generation by **1@MCM-41**,

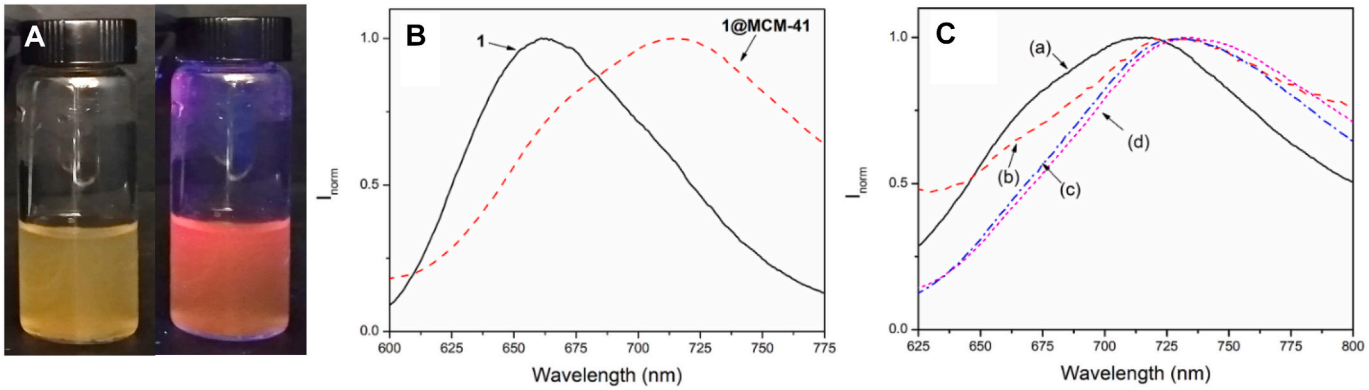

Fig. 4. (A) Aqueous suspension (PBS 10 mM, pH = 7) of **1@MCM-41** under visible light (left) and UV light (365 nm, right). (B) Normalized emission spectra (λ_{exc} = 420 nm) corresponding to **1** and **1@MCM-41** NPs in water (10 mM PBS, pH = 7). (C) Emission of **1@MCM-41** NPs (λ_{exc} = 420 nm) in different solvents: H_2O (a), CH_3CN (b), CH_2Cl_2 (c) and THF (d).

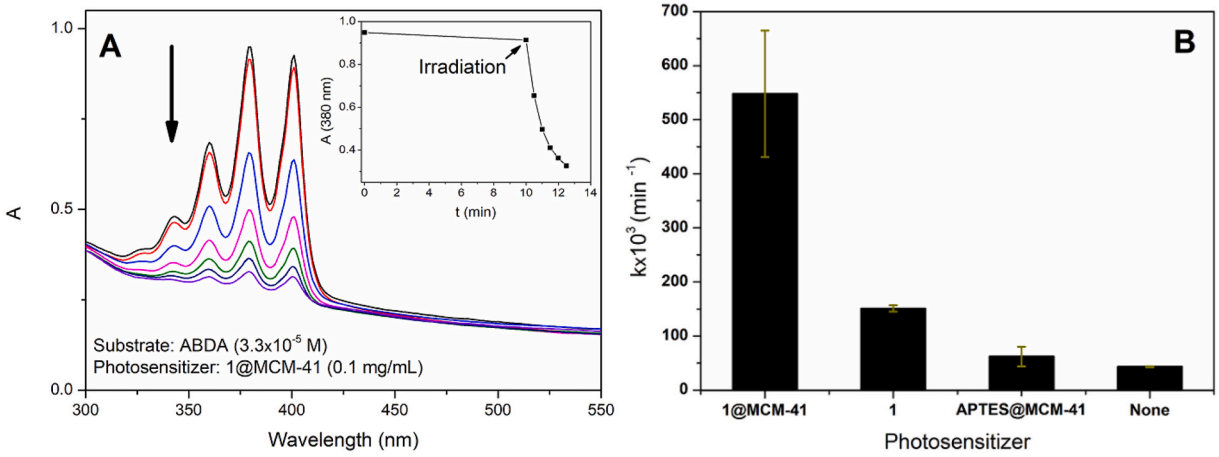

Fig. 5. (A) Irradiation of an aqueous solution of ABDA (3.3×10^{-5} M, PBS 10 mM, pH = 7) in the presence of **1@MCM-41** NPs (0.1 mg mL^{-1}). Inset: changes in the absorption, the arrow shows the time when irradiation was started. (B) Pseudo-first order rate constants for the photooxidation reaction of ABDA (3.3×10^{-5} M) in water (PBS 10 mM, pH = 7). The error was calculated as the standard deviation of at least three independent measurements.

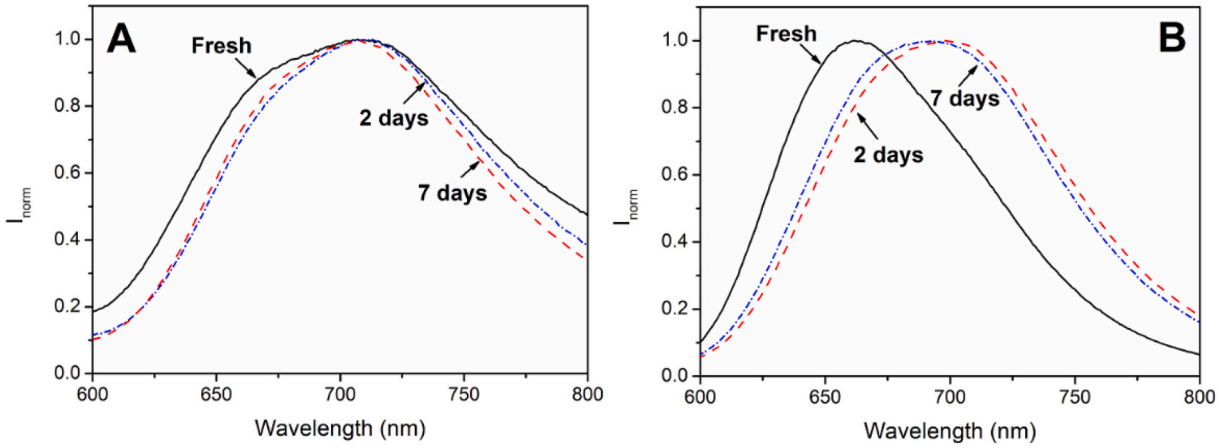

Fig. 6. Normalized emission spectra (λ_{exc} = 420 nm) of **1@MCM-41**, 0.1 mg mL^{-1} (A) and **1**, 2.9×10^{-5} M (B) as a function of time in water (PBS 10 mM, pH = 7).

the material was examined as a potential photodynamic anti-cancer agent, since hexamolybdenum clusters exhibit relevant photodynamic activity when incorporated into inorganic and organic materials [43,44,85]. Alternatively, the introduction of uncommon functional groups on the apical ligands has been also recently used to prepare free clusters that can accumulate in certain organelles of cancer cells and act as efficient PDT agents [41,86].

In a first step, the possible cytotoxicity of the hybrid material and the $(Bu_4N)_2[Mo_6I_8(CH_3CO_2)_6]$ complex was evaluated. The human cervical cancer HeLa cells and the human melanoma SK-Mel-103 cells were selected as tumoral models. The toxicity of complex **1** and **1@MCM-41** was evaluated at different concentrations at 24 h by the cell proliferation

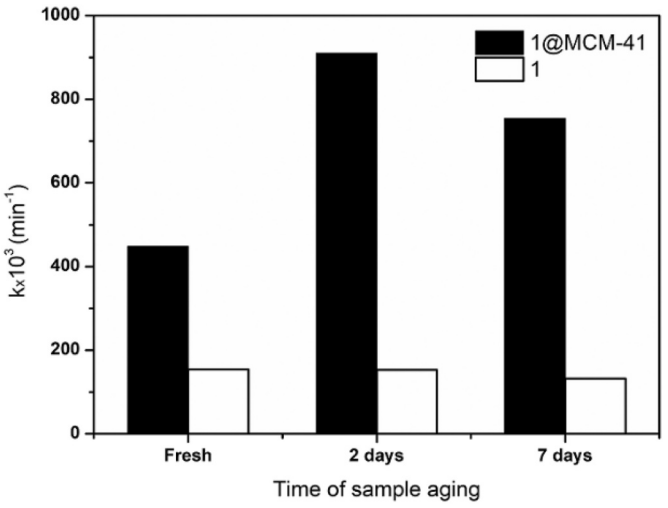

Fig. 7. Pseudo-first order rate constants for the photooxidation reaction of ABDA by samples of **1@MCM-41** and **1** stored in water (PBS 10 mM, pH = 7) at different times.

WST-1 assay. The nanoparticles and the complex were well-tolerated by both cell lines at concentrations up to 30 μM and 500 μg/mL **1** and **1@MCM-41** with viabilities in the 90–100 % range. (Figs. 8A and S7). Besides, crystal violet (CV) staining was performed for evaluating actively proliferating cells (see Figs. 8B and S6 and S7). The results demonstrated that there are no differences between control cells and those cells treated with the complex **1** and **1@MCM-41** and a similar number of proliferating cells in each field were observed. Images at higher magnifications revealed live cells with intact cell membranes in which the CV dye penetrated through the cytoplasm and stains the cell nuclei. All these findings confirmed that the compounds are well tolerated by the cells.

To discard any additional effect of complex **1** or the **1@MCM-41** nanoparticles to activate an immune response we carried out further studies with THP-1 cells. The cells were treated with the complex **1** and the **1@MCM-41** and their possible immunogenicity, i.e. the ability of a foreign substance to provoke an immune response in the body, was evaluated (i) by measuring the release of the intracellular lactate dehydrogenase (LDH) enzyme to the extracellular media as an inflammatory cell death marker, and (ii) by measuring inflammatory cytokine IL-1β release as indicative of the activation of an inflammatory response (Fig. 8C). In addition, THP-1 cells were stimulated with LPS and nigericin to active an inflammatory activation as control. The results

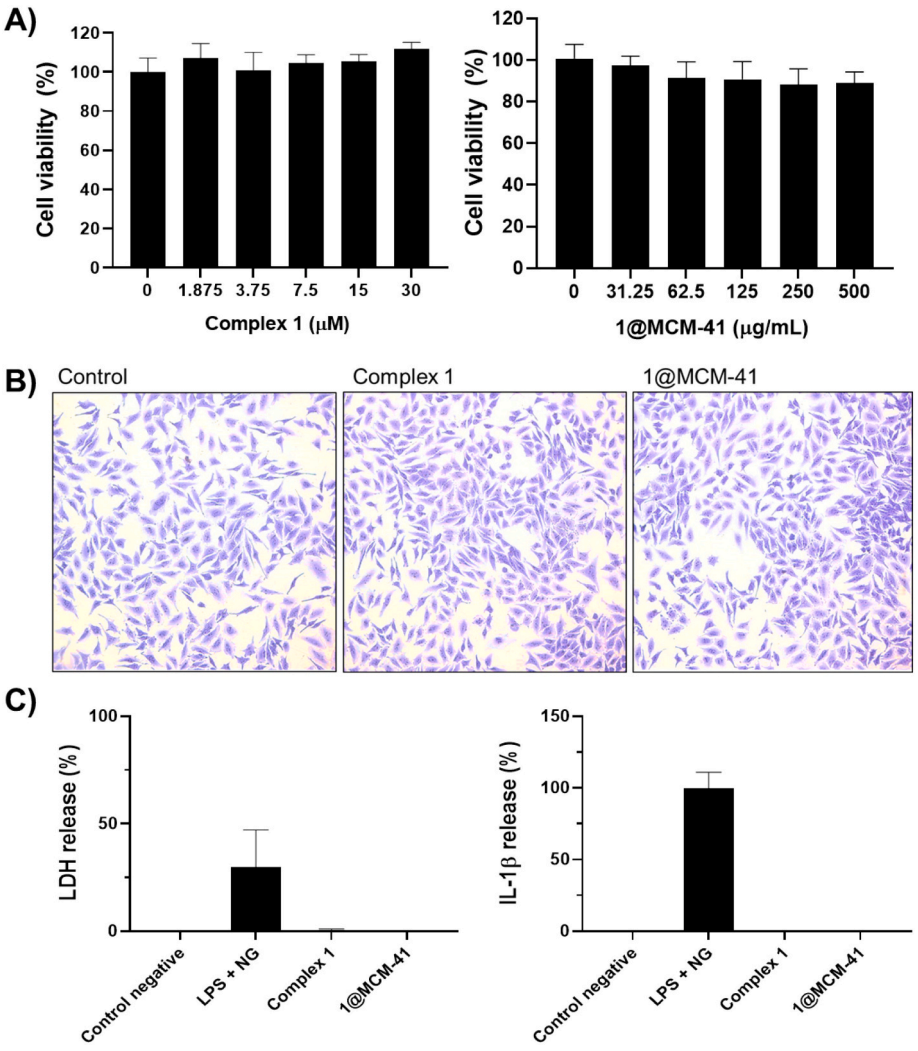

Fig. 8. (A) Cell viability assays at different concentrations of complex **1** (left) and **1@MCM-41** nanoparticles (right) at 24 h in HeLa cells. (B) Crystal violet staining of proliferative HeLa cells. (C) LDH and IL-1β release from THP-1 cells as immune activation markers. Data represent the mean ± SEM (standar error of the mean) of at least three independent experiments. (For interpretation of the references to colour in this figure legend, the reader is referred to the web version of this article.)

demonstrated that complex **1** and **1@MCM-41** are unable to induce a significant immune response.

Once confirmed no obvious toxicity effects on immune cells as well as in the studied cancer cells, the potential ability of our hybrid material for PDT was studied in cancer cells. HeLa cells were incubated with **1@MCM-41** nanoparticles, and with a solution of free cluster **1** (see Materials and methods section for details). Confocal laser scanning microscopy (CLSM) images revealed that **1@MCM-41** nanoparticles were efficiently internalized into the cells and the recorded emission intensity seems to indicate that the uptake was higher for **1@MCM-41** than for cluster **1** (Fig. 9). This is compatible with the uptake of the hybrid nanoparticles by endocytosis [43,48,64,65], whereas the anionic $[Mo_6I_8(CH_3CO_2)_6]^{2-}$ units of the free cluster are more impeded to enter through the membrane cell due to electrostatic repulsions [48]. Moreover, hydrolysis of the free complex that can originate micrometre-sized aggregates [53] can be also detrimental to its cellular internalization.

Once we assessed the proper uptake of **1@MCM-41** nanoparticles by HeLa cells, the toxicity of the material was tested in the dark or when irradiated (singlet oxygen generation). For this purpose, HeLa cells incubated with **1@MCM-41** nanoparticles (200 and 100 μg/mL) and with **1** (14.3 and 7.3 μM) were irradiated with a LED lamp at 400–700 nm for 20 min (Fig. 10). As a control, **MCM-41** or **APTES@MCM-41** were used at the same concentrations (200 and 100 μg/mL) in the dark or irradiated. The cell viability in the blank studies was found to be around 90–100 %, indicating that they are not cytotoxic. However, the results obtained with **1@MCM-41** were different and the hybrid

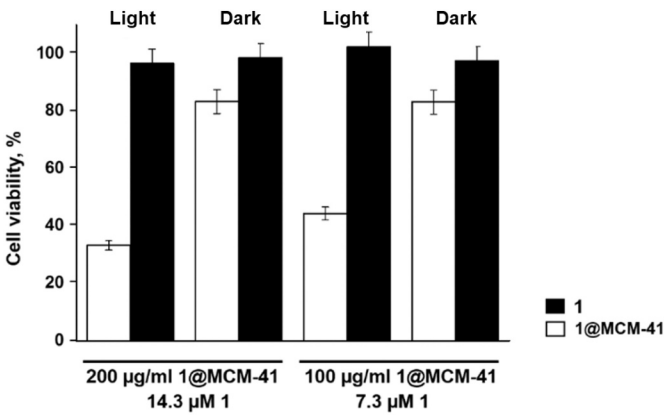

Fig. 10. Toxicity and phototoxicity of **1@MCM-41** and **1** against HeLa cells.

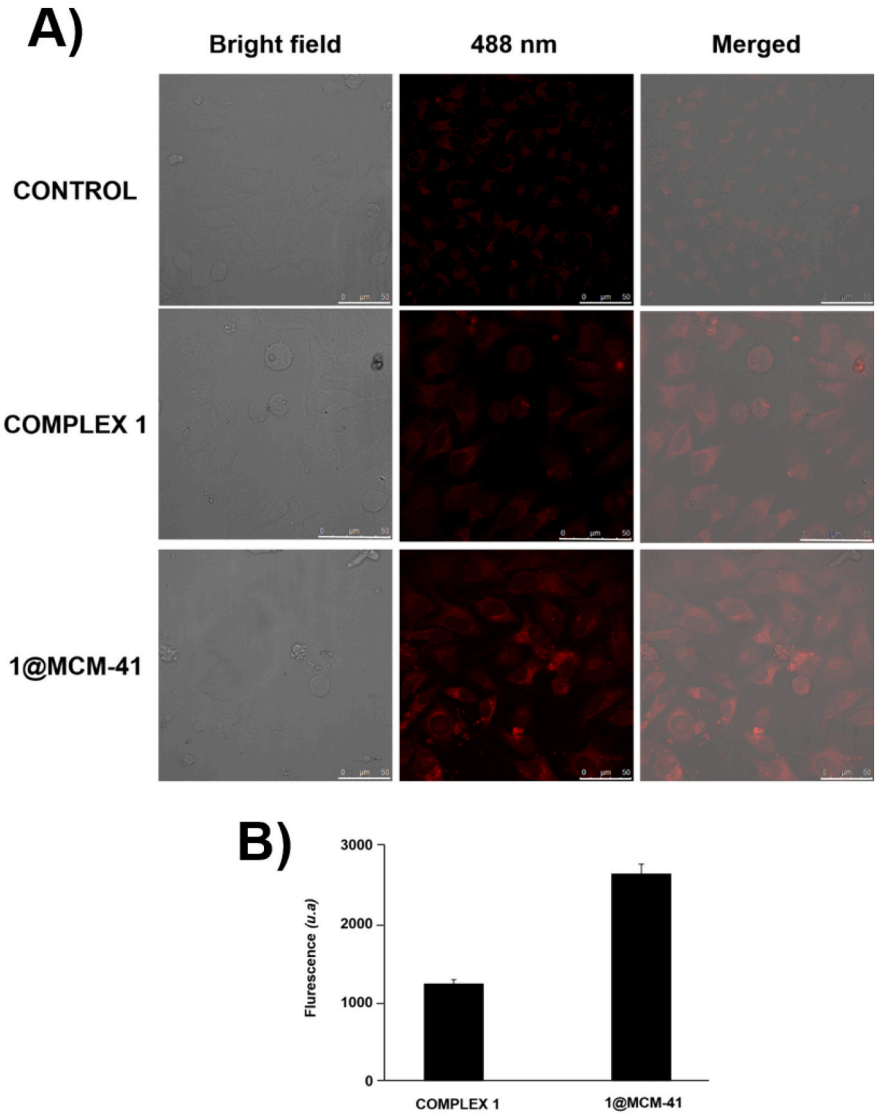

Fig. 9. (A) CLSM images showing the uptake of 50 μg/ mL of **1@MCM-41** and 3.5 μM of **1** by HeLa cells. (B) Quantification of complex associated fluorescence in cells using the ImageJ software. Error bars indicate standard deviations from two independent experiments.

nanoparticles demonstrated relevant photodynamic activity at both concentrations tested. In this respect, the viability of the HeLa cells incubated with the nanoparticles in the dark was found to be around 80–90 %, whereas upon irradiation the cell viability was reduced to 30–40 %. In the case of the free cluster **1**, at equivalent concentrations than in **1@MCM-41**, practically no photodynamic effect was observed.

The photodynamic activity was also evaluated against melanoma SK-Mel-103 cells (Fig. S8). In this case, the viability of SK-Mel-103 cells incubated with **1@MCM-41** also decreased under irradiation, although to a lesser extent than for HeLa cells (~60 % viability). Again, free cluster **1** showed practically no activity.

These results can be attributed to the poor cellular uptake of free cluster **1,** aggravated by hydrolysis processes that favour the precipitation of the photochemically active molybdenum cluster units, thus reducing their concentration and, therefore, its activity. Also, enzymatic degradation of the cluster inside the cell cannot be excluded. Dollo et al. found similar results for the cluster $(TBA)_2Mo_6Br_{14}$ which displayed no activity against A2780 cancer cells. The authors ascribed these results to poor cellular uptake and/or fast degradation of the cluster in the cell [44]. Our results demonstrate that encapsulation of cluster **1** in **MCM-41** favours the cellular uptake and protects the cluster against degradation. Moreover, the high dispersion of the cluster in the mesoporous silica guarantees good accessibility to oxygen and exposition to light, rendering the material a hybrid photosensitizer that generates efficiently singlet oxygen causing cellular death. These results are promising, and our efforts are now addressed to include cellular recognition vectors in the nanoparticles that can yield materials with improved PDT properties.

4. Conclusions

In summary, a new hybrid photosensitizer has been developed by electrostatic attachment of the hexanuclear molybdenum cluster $(Bu_4N)_2[Mo_6I_8(CH_3CO_2)_6]$ (**1**) to amino-modified mesoporous **MCM-41** silica nanoparticles. The high specific surface area of these nanoparticles (989 $m^2\ g^{-1}$) guarantees a very good dispersion of the hexamolybdenum cluster, as corroborated by electron microscopy analysis. The evaluation of the material as singlet oxygen photosensitizer was performed using the benchmark photooxidation reaction of 9,10-anthracenediyl-bis (methylene)dimalonic acid (ABDA) in water and the results indicate that the hybrid material generates singlet oxygen more efficiently than the free nanocluster even at lower concentration of the photoactive units. Finally, the potential activity of the new photosensitizer for PDT was tested in cancer cells. The possible toxicity of the complex **1** and the **1@MCM-41** was discarded in cancer cells as well as any additional effect to activate an immune response. The hybrid nanoparticles exhibit good activity against human cervical cancer (HeLa) cells and moderate activity against melanoma (SK-Mel-103) cells whereas free cluster **1** showed practically no photoactivity, probably due to poor cellular uptake and degradation inside the cell. The work presented here shows a new strategy to develop efficient photosensitizer materials by a combination of hexanuclear molybdenum clusters and mesoporous silica nanoparticles. The high porosity of the nanoparticles guarantees a good dispersion of the cluster, which favours its photosensitizing properties. Moreover, the nanoparticles protect the cluster from hydrolysis and subsequent precipitation and facilitate cellular uptake, which is very convenient in PDT applications. Additional work is being performed in our laboratories to optimize the nanoparticle design and attachment of the molybdenum photoactive units and render efficient photosensitizers against different types of cancer cells.

CRediT authorship contribution statement

Cristina de la Torre: investigation, writing - original draft; Raquel Gavara: investigation, writing - original draft; Alba García-Fernández: investigation, writing; Maxim Mikhaylov: investigation; Maxim N. Sokolov: conceptualization, writing - review & editing; Juan F. Miravet: conceptualization; Félix Sancenón: conceptualization, supervision, writing - review & editing; Ramón Martínez-Máñez: conceptualization, funding acquisition; writing - review & editing; Francisco Galindo: conceptualization, supervision, funding acquisition; writing -review & editing.

Declaration of competing interest

The authors declare no competing financial interest.

Data availability

Data will be made available on request.

Acknowledgements

Ministerio de Ciencia, Innovación y Universidades of Spain (grant RTI2018-101675-B-I00) is acknowledged. F.G. thanks Universitat Jaume I (grant UJI-B2021-51) for the financial support. R.M.-M. laboratory members thank the financial support from the Spanish Government (project RTI2018-100910-B-C41) and the Generalitat Valenciana (project PROMETEO 2018/024). The research was supported by the Ministry of Science and Higher Education of the Russian Federation (M. N.S.). C.T. acknowledges the Generalitat Valenciana for her postdoctoral fellowship (APOSTD/2019/121). R.G. thanks Universitat Jaume I for a postdoctoral fellowship (POSTDOC-B/2018/09). We would like to thank Prof. Iván Mora-Seró (INAM-UJI) for the singlet oxygen phosphorescence measurements. The help of Jean Colombari in the final phase of this work is also recognized. SCIC-UJI is acknowledged for the technical support.

Appendix A. Supplementary data

Supplementary information is available and free of charge: Powder X-ray diffraction pattern of as made **MCM-41**, calcined **MCM-41** and final solid **1@MCM-41**; Hydrodynamic size and ζ Potential of **MCM-41**, **APTES@MCM-41** and **1@MCM-41**; Emission spectra of **1** and **1@MCM-41** corresponding to air-equilibrated solutions and the same solutions after bubbling oxygen for 15 min; Pseudo-first order fittings for the photooxidation reaction of ABDA; Singlet oxygen phosphorescence recorded for oxygen saturated CH_3CN solutions of **1** and anthracene; Crystal violet staining of HeLa and SK-Mel-103 in the presence of **1@MCM-41** and **1**; Toxicity and phototoxicity of **1@MCM-41** and **1** against SK-Mel-103 cells. Supplementary data to this article can be found online at https://doi.org/10.1016/j.bioadv.2022.213057.

References

[1] T. Zhang, G. Xing, W. Chen, L. Chen, Porous organic polymers: a promising platform for efficient photocatalysis, Mater. Chem. Front. 4 (2020) 332–353, https://doi.org/10.1039/c9qm00633h.
[2] S. Lacombe, T. Pigot, Materials for selective photo-oxygenation vs. photocatalysis: preparation, properties and applications in environmental and health fields, Catal. Sci. Technol. 6 (2016) 1571–1592, https://doi.org/10.1039/c5cy01929j.
[3] E. Arzoumanian, F. Ronzani, A. Trivella, E. Oliveros, M. Sarakha, C. Richard, S. Blanc, T. Pigot, S. Lacombe, Transparent organosilica photocatalysts activated by visible light: photophysical and oxidative properties at the gas-solid interface, ACS Appl. Mater. Interfaces 6 (2014) 275–288, https://doi.org/10.1021/am404175y.
[4] M.L. Marin, L. Santos-Juanes, A. Arques, A.M. Amat, M.A. Miranda, Organic photocatalysts for the oxidation of pollutants and model compounds, Chem. Rev. 112 (2012) 1710–1750, https://doi.org/10.1021/cr2000543.
[5] N. MacIa, R. Bresoli-Obach, S. Nonell, B. Heyne, Hybrid silver nanocubes for improved plasmon-enhanced singlet oxygen production and inactivation of bacteria, J. Am. Chem. Soc. 141 (2019) 684–692, https://doi.org/10.1021/jacs.8b12206.
[6] F. Cieplik, D. Deng, W. Crielaard, W. Buchalla, E. Hellwig, A. Al-Ahmad, T. Maisch, Antimicrobial photodynamic therapy–what we know and what we don't, Crit. Rev. Microbiol. 44 (2018) 571–589, https://doi.org/10.1080/1040841X.2018.1467876.

[7] A. Rineh, N.K. Dolla, A.R. Ball, M. Magana, J.B. Bremner, M.R. Hamblin, G. P. Tegos, M.J. Kelso, Attaching the NorA efflux pump inhibitor INF55 to methylene blue enhances antimicrobial photodynamic inactivation of methicillin-resistant Staphylococcus aureus in vitro and in vivo, ACS Infect. Dis. 3 (2017) 756–766, https://doi.org/10.1021/acsinfecdis.7b00095.

[8] C. Felip-León, C. Arnau Del Valle, V. Pérez-Laguna, M. Isabel Millán-Lou, J. F. Miravet, M. Mikhailov, M.N. Sokolov, A. Rezusta-López, F. Galindo, Superior performance of macroporous over gel type polystyrene as a support for the development of photo-bactericidal materials, J. Mater. Chem. B 5 (2017) 6058–6064, https://doi.org/10.1039/c7tb01478c.

[9] A. Beltrán, M. Mikhailov, M.N. Sokolov, V. Pérez-Laguna, A. Rezusta, M.J. Revillo, F. Galindo, A photobleaching resistant polymer supported hexanuclear molybdenum iodide cluster for photocatalytic oxygenations and photodynamic inactivation of: Staphylococcus aureus, J. Mater. Chem. B 4 (2016) 5975–5979, https://doi.org/10.1039/c6tb01966h.

[10] M. Lan, S. Zhao, W. Liu, C.S. Lee, W. Zhang, P. Wang, Photosensitizers for photodynamic therapy, Adv. Healthc. Mater. 8 (2019) 1–37, https://doi.org/10.1002/adhm.201900132.

[11] C. Felip-León, O. Martínez-Arroyo, S. Díaz-Oltra, J.F. Miravet, N. Apostolova, F. Galindo, Synthesis, spectroscopic studies and biological evaluation of acridine derivatives: the role of aggregation on the photodynamic efficiency, Bioorg. Med. Chem. Lett. 28 (2018) 869–874, https://doi.org/10.1016/j.bmcl.2018.02.005.

[12] M.K. Kuimova, S.W. Botchway, A.W. Parker, M. Balaz, H.A. Collins, H.L. Anderson, K. Suhling, P.R. Ogilby, Imaging intracellular viscosity of a single cell during photoinduced cell death, Nat. Chem. 1 (2009) 69–73, https://doi.org/10.1038/nchem.120.

[13] A. Szokalska, M. Makowski, D. Nowis, G.M. Wilczyński, M. Kujawa, C. Wójcik, I. Młynarczuk-Biały, P. Salwa, J. Bil, S. Janowska, P. Agostinis, T. Verfaillie, M. Bugajski, J. Gietka, T. Issat, E. Głodkowska, P. Mrówka, T. Stoklosa, M. R. Hamblin, P. Mróz, M. Jakóbisiak, J. Golab, Proteasome inhibition potentiates antitumor effects of photodynamic therapy in mice through induction of endoplasmic reticulum stress and unfolded protein response, Cancer Res. 69 (2009) 4235–4243, https://doi.org/10.1158/0008-5472.CAN-08-3439.

[14] M.I. Burguete, F. Galindo, R. Gavara, S.V. Luis, M. Moreno, P. Thomas, D. A. Russell, Singlet oxygen generation using a porous monolithic polymer supported photosensitizer: potential application to the photodynamic destruction of melanoma cells, Photochem. Photobiol. Sci. 8 (2009) 37–44, https://doi.org/10.1039/b810921d.

[15] F. Thorning, F. Jensen, P.R. Ogilby, Modeling the effect of solvents on nonradiative singlet oxygen deactivation: going beyond weak coupling in intermolecular electronic-to-vibrational energy transfer, ACS Appl. Mater. Interfaces (2020), https://doi.org/10.1021/acs.jpcb.0c00807.

[16] M. Bregnhøj, M. Westberg, B.F. Minaev, P.R. Ogilby, Singlet oxygen photophysics in liquid solvents: converging on a unified picture, Acc. Chem. Res. 50 (2017) 1920–1927, https://doi.org/10.1021/acs.accounts.7b00169.

[17] P.R. Ogilby, Singlet oxygen: there is indeed something new under the sun, Chem. Soc. Rev. 39 (2010) 3181–3209, https://doi.org/10.1039/b926014p.

[18] C. Schweitzer, R. Schmidt, Physical mechanisms of generation and deactivation of singlet oxygen, Chem. Rev. 103 (2003) 1685–1757, https://doi.org/10.1021/cr010371d.

[19] A.W. Maverick, J.S. Najdzionek, D. MacKenzie, D.G. Nocera, H.B. Gray, Spectroscopic, electrochemical, and photochemical properties of molybdenum(II) and tungsten(II) halide clusters, J. Am. Chem. Soc. 105 (1983) 1878–1882, https://doi.org/10.1021/ja00345a034.

[20] J.A. Jackson, C. Turro, M.D. Newsham, D.G. Nocera, Oxygen quenching of electronically excited hexanuclear mdybdenum and tungsten halide clusters, J. Phys. Chem. 94 (1990) 4500–4507.

[21] N. Prokopuk, D.F. Shriver, The octahedral M6Y8 and M6Y12 clusters of group 4 and 5 transition metals, Adv. Inorg. Chem. 46 (1998) 1–49, https://doi.org/10.1016/S0898-8838(08)60148-8.

[22] K. Kirakci, P. Kubát, J. Langmaier, T. Polívka, M. Fuciman, K. Fejfarová, K. Lang, A comparative study of the redox and excited state properties of (nBu 4 N) 2 [Mo 6 X 14] and (nBu 4 N) 2 [Mo 6 X 8 (CF 3 COO) 6] (X = Cl, Br, or I), Dalton Trans. 42 (2013) 7224–7232, https://doi.org/10.1039/c3dt32863e.

[23] M.A. Mikhaylov, M.N. Sokolov, Molybdenum iodides – from obscurity to bright luminescence, Eur. J. Inorg. Chem. 2019 (2019) 4181–4197, https://doi.org/10.1002/ejic.201900630.

[24] T.K.N. Nguyen, F. Grasset, S. Cordier, M. Amela-Cortes, Y. Matsui, N. Ohashi, N. Shirahata, T. Uchikoshi, Preparation and characterization of hollow silica nanocomposite functionalized with UV absorbable molybdenum cluster, Adv. Powder Technol. 31 (2020) 895–903, https://doi.org/10.1016/j.apt.2019.12.009.

[25] M. Amela-Cortes, S. Paofai, S. Cordier, H. Folliot, Y. Molard, Tuned red NIR phosphorescence of polyurethane hybrid composites embedding metallic nanoclusters for oxygen sensing, Chem. Commun. 51 (2015) 8177–8180, https://doi.org/10.1039/c5cc01867f.

[26] R.N. Ghosh, G.L. Baker, C. Ruud, D.G. Nocera, Fiber-optic oxygen sensor using molybdenum chloride cluster luminescence, Appl. Phys. Lett. 75 (1999) 2885–2887, https://doi.org/10.1063/1.125180.

[27] E. Ferreira Molina, N.A. Martins de Jesus, S. Paofai, P. Hammer, M. Amela-Cortes, M. Robin, S. Cordier, Y. Molard, When a red–NIR-emissive Cs2[Mo6Br14] interacts with an active diureasil–PEO matrix: design of tunable and white-light-emitting hybrid material, Chem. Eur. J. 25 (2019) 15248–15251, https://doi.org/10.1002/chem.201903892.

[28] M. Robin, N. Dumait, M. Amela-Cortes, C. Roiland, M. Harnois, E. Jacques, H. Folliot, Y. Molard, Direct integration of red-NIR emissive ceramic-like AnM6Xi8Xa6 metal cluster salts in organic copolymers using supramolecular interactions, Chem. Eur. J. 24 (2018) 4825–4829, https://doi.org/10.1002/chem.201800860.

[29] O.A. Efremova, K.A. Brylev, Y.A. Vorotnikov, L. Vejsadová, M.A. Shestopalov, G. F. Chimonides, P. Mikes, P.D. Topham, S.J. Kim, N. Kitamura, A.J. Sutherland, Photoluminescent materials based on PMMA and a highly-emissive octahedral molybdenum metal cluster complex, J. Mater. Chem. C 4 (2016) 497–503, https://doi.org/10.1039/c5tc03204k.

[30] K. Kirakci, V. Šícha, J. Holub, P. Kubát, K. Lang, Luminescent hydrogel particles prepared by self-assembly of β-cyclodextrin polymer and octahedral molybdenum cluster complexes, Inorg. Chem. 53 (2014) 13012–13018, https://doi.org/10.1021/ic502144z.

[31] T. Aubert, F. Cabello-Hurtado, M.A. Esnault, C. Neaime, D. Lebret-Chauvel, S. Jeanne, P. Pellen, C. Roiland, L. Le Polles, N. Saito, K. Kimoto, H. Haneda, N. Ohashi, F. Grasset, S. Cordier, Extended investigations on luminescent Cs2 [Mo6Br 14]@SiO2 nanoparticles: physico-structural characterizations and toxicity studies, J. Phys. Chem. C 117 (2013) 20154–20163, https://doi.org/10.1021/jp405836q.

[32] T.G. Truong, B. Dierre, F. Grasset, N. Saito, N. Saito, T.K.N. Nguyen, K. Takahashi, T. Uchikoshi, M. Amela-Cortes, Y. Molard, S. Cordier, N. Ohashi, Visible tunable lighting system based on polymer composites embedding ZnO and metallic clusters: from colloids to thin films, Sci. Technol. Adv. Mater. 17 (2016) 443–453, https://doi.org/10.1080/14686996.2016.1202724.

[33] M. Prévôt, M. Amela-Cortes, S.K. Manna, R. Lefort, S. Cordier, H. Folliot, L. Dupont, Y. Molard, Design and integration in electro-optic devices of highly efficient and robust red-NIR phosphorescent nematic hybrid liquid crystals containing [Mo6I8(OCOCnF2n+1)6]2- (n = 1, 2, 3) nanoclusters, Adv. Funct. Mater. 25 (2015) 4966–4975, https://doi.org/10.1002/adfm.201501876.

[34] C. Neaime, M. Amela-Cortes, F. Grasset, Y. Molard, S. Cordier, B. Dierre, M. Mortier, T. Takei, K. Takahashi, H. Haneda, M. Verelst, S. Lechevallier, Time-gated luminescence bioimaging with new luminescent nanocolloids based on [Mo 6 I 8 (C 2 F 5 COO) 6] 2− metal atom clusters, Phys. Chem. Chem. Phys. 18 (2016) 30166–30173, https://doi.org/10.1039/c6cp05290h.

[35] Y.A. Vorotnikov, T.N. Pozmogova, A.O. Solovieva, S.M. Miroshnichenko, E. V. Vorontsova, L.V. Shestopalova, Y.V. Mironov, M.A. Shestopalov, O.A. Efremova, Luminescent silica mesoparticles for protein transduction, Mater. Sci. Eng. C 96 (2019) 530–538, https://doi.org/10.1016/j.msec.2018.11.056.

[36] M.N. Ivanova, Y.A. Vorotnikov, E.E. Plotnikova, M.V. Marchuk, A.A. Ivanov, I. P. Asanov, A.R. Tsygankova, E.D. Grayfer, V.E. Fedorov, M.A. Shestopalov, Hexamolybdenum clusters supported on exfoliated h-BN nanosheets for photocatalytic water purification, Inorg. Chem. 59 (2020) 6439–6448, https://doi.org/10.1021/acs.inorgchem.0c00528.

[37] A.A. Petunin, D.V. Evtushok, N.A. Vorotnikova, N.V. Kuratieva, Y.A. Vorotnikov, M.A. Shestopalov, Hexasubstituted iodide tungsten cluster complexes with azide and isothiocyanate ligands, Eur. J. Inorg. Chem. 2020 (2020) 2177–2181, https://doi.org/10.1002/ejic.202000204.

[38] M. Feliz, P. Atienzar, M. Amela-Cortés, N. Dumait, P. Lemoine, Y. Molard, S. Cordier, Supramolecular anchoring of octahedral molybdenum clusters onto graphene and their synergies in photocatalytic water reduction, Inorg. Chem. 58 (2019) 15443–15454, https://doi.org/10.1021/acs.inorgchem.9b02529.

[39] E.D. Novikova, Y.A. Vorotnikov, N.A. Nikolaev, A.R. Tsygankova, M. A. Shestopalov, O.A. Efremova, Synergetic effect of Mo6 clusters and gold nanoparticles on the photophysical properties of both components, Chem. Eur. J. 27 (2021) 2818–2825, https://doi.org/10.1002/chem.202004618.

[40] E.D. Novikova, Y.A. Vorotnikov, N.A. Nikolaev, A.R. Tsygankova, M. A. Shestopalov, O.A. Efremova, The role of gold nanoparticles' aspect ratio in plasmon-enhanced luminescence and the singlet oxygen generation rate of Mo6clusters, Chem. Commun. 57 (2021) 7770–7773, https://doi.org/10.1039/d1cc03347f.

[41] K. Kirakci, J. Zelenka, M. Rumlová, J. Cvačka, T. Ruml, K. Lang, Cationic octahedral molybdenum cluster complexes functionalized with mitochondria-targeting ligands: photodynamic anticancer and antibacterial activities, Biomater. Sci. 7 (2019) 1386–1392, https://doi.org/10.1039/c8bm01564c.

[42] N.A. Vorotnikova, A.Y. Alekseev, Y.A. Vorotnikov, D.V. Evtushok, Y. Molard, M. Amela-Cortes, S. Cordier, A.I. Smolentsev, C.G. Burton, P.M. Kozhin, P. Zhu, P. D. Topham, Y.V. Mironov, M. Bradley, O.A. Efremova, M.A. Shestopalov, Octahedral molybdenum cluster as a photoactive antimicrobial additive to a fluoroplastic, Mater. Sci. Eng. C 105 (2019), 110150, https://doi.org/10.1016/j.msec.2019.110150.

[43] J. Elistratova, A. Mukhametshina, K. Kholin, I. Nizameev, M. Mikhailov, M. Sokolov, R. Khairullin, R. Miftakhova, G. Shammas, M. Kadirov, K. Petrov, A. Rizvanov, A. Mustafina, Interfacial uploading of luminescent hexamolybdenum cluster units onto amino-decorated silica nanoparticles as new design of nanomaterial for cellular imaging and photodynamic therapy, J. Colloid Interface Sci. 538 (2019) 387–396, https://doi.org/10.1016/j.jcis.2018.12.013.

[44] N. Brandhonneur, T. Hatahet, M. Amela-Cortes, Y. Molard, S. Cordier, G. Dollo, Molybdenum cluster loaded PLGA nanoparticles: an innovative theranostic approach for the treatment of ovarian cancer, Eur. J. Pharm. Biopharm. 125 (2018) 95–105, https://doi.org/10.1016/j.ejpb.2018.01.007.

[45] K. Kirakci, J. Zelenka, M. Rumlová, J. Martinčík, M. Nikl, T. Ruml, K. Lang, Octahedral molybdenum clusters as radiosensitizers for X-ray induced photodynamic therapy, J. Mater. Chem. B 6 (2018) 4301–4307, https://doi.org/10.1039/C8TB00893K.

[46] A.M. Cheplakova, A.O. Solovieva, T.N. Pozmogova, Y.A. Vorotnikov, K.A. Brylev, N.A. Vorotnikova, E.V. Vorontsova, Y.V. Mironov, A.F. Poveshchenko, K. A. Kovalenko, M.A. Shestopalov, Nanosized mesoporous metal–organic framework MIL-101 as a nanocarrier for photoactive hexamolybdenum cluster compounds,

J. Inorg. Biochem. 166 (2017) 100–107, https://doi.org/10.1016/j.jinorgbio.2016.11.014.
[47] E.V. Svezhentseva, A.O. Solovieva, Y.A. Vorotnikov, O.G. Kurskaya, K.A. Brylev, A. R. Tsygankova, M.V. Edeleva, S.N. Gyrylova, N. Kitamura, O.A. Efremova, M. A. Shestopalov, Y.V. Mironov, A.M. Shestopalov, Water-soluble hybrid materials based on {Mo 6 X 8 } 4+ (X = Cl, Br, I) cluster complexes and sodium polystyrene sulfonate, New J. Chem. 41 (2017) 1670–1676, https://doi.org/10.1039/c6nj03469a.
[48] A.O. Solovieva, Y.A. Vorotnikov, K.E. Trifonova, O.A. Efremova, A.A. Krasilnikova, K.A. Brylev, E.V. Vorontsova, P.A. Avrorov, L.V. Shestopalova, A.F. Poveshchenko, Y.V. Mironov, M.A. Shestopalov, Cellular internalisation, bioimaging and dark and photodynamic cytotoxicity of silica nanoparticles doped by {Mo 6 I 8 } 4+ metal clusters, J. Mater. Chem. B 4 (2016) 4839–4846, https://doi.org/10.1039/c6tb00723f.
[49] S. Fedorenko, J. Elistratova, A. Stepanov, A. Khazieva, M. Mikhailov, M. Sokolov, K. Kholin, I. Nizameev, R. Mendes, M. Rümmeli, T. Gemming, B. Weise, L. Giebeler, D. Mikhailova, S. Dutz, D. Zahn, A. Voloshina, A. Sapunova, A. Daminova, S. Fedosimova, A. Mustafina, ROS-generation and cellular uptake behavior of amino-silica nanoparticles arisen from their uploading by both iron-oxides and hexamolybdenum clusters, Mater. Sci. Eng. C 117 (2020), https://doi.org/10.1016/j.msec.2020.111305.
[50] M.A. Mikhaylov, P.A. Abramov, V.Y. Komarov, M.N. Sokolov, Cluster aqua/hydroxocomplexes supporting extended hydrogen bonding networks. Preparation and structure of a unique series of cluster hydrates [Mo6I8(OH)4(H2O)2]·nH2O (n = 2, 12, 14), Polyhedron 122 (2017) 241–246, https://doi.org/10.1016/j.poly.2016.11.011.
[51] Y.A. Vorotnikov, O.A. Efremova, I.N. Novozhilov, V.V. Yanshole, N.V. Kuratieva, K. A. Brylev, N. Kitamura, Y.V. Mironov, M.A. Shestopalov, Hexaazide octahedral molybdenum cluster complexes: synthesis, properties and the evidence of hydrolysis, J. Mol. Struct. 1134 (2017) 237–243, https://doi.org/10.1016/j.molstruc.2016.12.052.
[52] K. Kirakci, P. Kubát, M. Kučeráková, V. Šícha, H. Gbelcová, P. Lovecká, P. Grznárová, T. Ruml, K. Lang, Water-soluble octahedral molybdenum cluster compounds Na2[Mo6I8(N3)6] and Na2[Mo6I8(NCS)6]: syntheses, luminescence, and in vitro studies, Inorg. Chim. Acta 441 (2016) 42–49, https://doi.org/10.1016/j.ica.2015.10.043.
[53] T. Aubert, A. Burel, M.A. Esnault, S. Cordier, F. Grasset, F. Cabello-Hurtado, Root uptake and phytotoxicity of nanosized molybdenum octahedral clusters, J. Hazard. Mater. 219–220 (2012) 111–118, https://doi.org/10.1016/j.jhazmat.2012.03.058.
[54] N. Brandhonneur, Y. Boucaud, A. Verger, N. Dumait, Y. Molard, S. Cordier, G. Dollo, Molybdenum cluster loaded PLGA nanoparticles as efficient tools against epithelial ovarian cancer, Int. J. Pharm. 592 (2021), 120079, https://doi.org/10.1016/j.ijpharm.2020.120079.
[55] T.T. Hoang Thi, V. Du Cao, T.N.Q. Nguyen, D.T. Hoang, V.C. Ngo, D.H. Nguyen, Functionalized mesoporous silica nanoparticles and biomedical applications, Mater. Sci. Eng. C 99 (2019) 631–656, https://doi.org/10.1016/j.msec.2019.01.129.
[56] S. Bayir, A. Barras, R. Boukherroub, S. Szunerits, L. Raehm, S. Richeter, J. O. Durand, Mesoporous silica nanoparticles in recent photodynamic therapy applications, Photochem. Photobiol. Sci. 17 (2018) 1651–1674, https://doi.org/10.1039/c8pp00143j.
[57] C. Giménez, C. De La Torre, M. Gorbe, E. Aznar, F. Sancenón, J.R. Murguía, R. Martínez-Máñez, M.D. Marcos, P. Amorós, Gated mesoporous silica nanoparticles for the controlled delivery of drugs in cancer cells, Langmuir. 31 (2015) 3753–3762, https://doi.org/10.1021/acs.langmuir.5b00139.
[58] C. De La Torre, L. Mondragón, C. Coll, F. Sancenón, M.D. Marcos, R. Martínez-Máñez, P. Amorós, E. Pérez-Payá, M. Orzáez, Cathepsin-B induced controlled release from peptide-capped mesoporous silica nanoparticles, Chem. Eur. J. 20 (2014) 15309–15314, https://doi.org/10.1002/chem.201404382.
[59] E. Aznar, R. Villalonga, C. Giménez, F. Sancenón, M.D. Marcos, R. Martínez-Máñez, P. Díez, J.M. Pingarrón, P. Amorós, Glucose-triggered release using enzyme-gated mesoporous silica nanoparticles, Chem. Commun. 49 (2013) 6391–6393, https://doi.org/10.1039/c3cc42210k.
[60] C. Graf, Q. Gao, I. Schütz, C.N. Noufele, W. Ruan, U. Posselt, E. Korotianskiy, D. Nordmeyer, F. Rancan, S. Hadam, A. Vogt, J. Lademann, V. Haucke, E. Rühl, Surface functionalization of silica nanoparticles supports colloidal stability in physiological media and facilitates internalization in cells, Langmuir. 28 (2012) 7598–7613, https://doi.org/10.1021/la204913t.
[61] A. García-Fernández, E. Aznar, R. Martínez-Máñez, F. Sancenón, New advances in in vivo applications of gated mesoporous silica as drug delivery nanocarriers, Small. 16 (2020) 1–62, https://doi.org/10.1002/smll.201902242.
[62] I. Slowing, B.G. Trewyn, V.S.Y. Lin, Effect of surface functionalization of MCM-41-type mesoporous silica nanoparticles on the endocytosis by human cancer cells, J. Am. Chem. Soc. 128 (2006) 14792–14793, https://doi.org/10.1021/ja0645943.
[63] A. Nel, T. Xia, L. Mädler, N. Li, Toxic potential of materials at the nanolevel, Science (80-.) 311 (2006) 622–627, https://doi.org/10.1126/science.1114397.
[64] S.H. Cheng, C.H. Lee, C.S. Yang, F.G. Tseng, C.Y. Mou, L.W. Lo, Mesoporous silica nanoparticles functionalized with an oxygen-sensing probe for cell photodynamic therapy: potential cancer theranostics, J. Mater. Chem. 19 (2009) 1252–1257, https://doi.org/10.1039/b816636f.
[65] H.L. Tu, Y.S. Lin, H.Y. Lin, Y. Hung, L.W. Lo, Y.F. Chen, C.Y. Mou, In vitro studies of functionalized mesoporous silica nanoparticles for photodynamic therapy, Adv. Mater. 21 (2009) 172–177, https://doi.org/10.1002/adma.200800548.
[66] D. Brevet, M. Gary-Bobo, L. Raehm, S. Richeter, O. Hocine, K. Amro, B. Loock, P. Couleaud, C. Frochot, A. Morère, P. Maillard, M. Garcia, J.O. Durand, Mannose-targeted mesoporous silica nanoparticles for photodynamic therapy, Chem. Commun. (2009) 1475–1477, https://doi.org/10.1039/b900427k.
[67] N. Clemente, I. Miletto, E. Gianotti, M. Invernizzi, L. Marchese, U. Dianzani, F. Renò, Verteporfin-loaded mesoporous silica nanoparticles inhibit mouse melanoma proliferation in vitro and in vivo, J. Photochem. Photobiol. B Biol. 197 (2019), 111533, https://doi.org/10.1016/j.jphotobiol.2019.111533.
[68] J.L. Vivero-Escoto, M. Elnagheeb, Mesoporous silica nanoparticles loaded with cisplatin and phthalocyanine for combination chemotherapy and photodynamic therapy in vitro, Nanomaterials. 5 (2015) 2302–2316, https://doi.org/10.3390/nano5042302.
[69] E. Ricci-Junior, L.B. de Oliveira de Siqueira, R.A.S. Rodrigues, F. Sancenón, R. Martínez-Máñez, J.A. de Moraes, R. Santos-Oliveira, Nanocarriers as phototherapeutic drug delivery system: appraisal of three different nanosystems in an in vivo and in vitro exploratory study, Photodiagn. Photodyn. Ther. 21 (2018) 43–49, https://doi.org/10.1016/j.pdpdt.2017.11.003.
[70] J. Zhan, Z. Ma, D. Wang, X. Li, X. Li, L. Le, A. Kang, P. Hu, L. She, F. Yang, Magnetic and pH dual-responsive mesoporous silica nanocomposites for effective and low-toxic photodynamic therapy, Int. J. Nanomedicine 12 (2017) 2733–2748, https://doi.org/10.2147/IJN.S127528.
[71] I. Miletto, A. Fraccarollo, N. Barbero, C. Barolo, M. Cossi, L. Marchese, E. Gianotti, Mesoporous silica nanoparticles incorporating squaraine-based photosensitizers: a combined experimental and computational approach, Dalton Trans. 47 (2018) 3038–3046, https://doi.org/10.1039/c7dt03735j.
[72] M.A. Mikhailov, K.A. Brylev, P.A. Abramov, E. Sakuda, S. Akagi, A. Ito, N. Kitamura, M.N. Sokolov, Synthetic tuning of redox, spectroscopic, and photophysical properties of {Mo6I8}4+ core cluster complexes by terminal carboxylate ligands, Inorg. Chem. 55 (2016) 8437–8445, https://doi.org/10.1021/acs.inorgchem.6b01042.
[73] C. Arnau Del Valle, C. Felip-León, C.A. Angulo-Pachón, M. Mikhailov, M. N. Sokolov, J.F. Miravet, F. Galindo, Photoactive hexanuclear molybdenum nanoclusters embedded in molecular organogels, Inorg. Chem. 58 (2019) 8900–8905, https://doi.org/10.1021/acs.inorgchem.9b00916.
[74] M. Amela-Cortes, Y. Molard, S. Paofai, A. Desert, J.L. Duvail, N.G. Naumov, S. Cordier, Versatility of the ionic assembling method to design highly luminescent PMMA nanocomposites containing [M6Qi8La6]n- octahedral nano-building blocks, Dalton Trans. 45 (2016) 237–245, https://doi.org/10.1039/c5dt03734d.
[75] M. Amela-Cortes, A. Garreau, S. Cordier, E. Faulques, J.L. Duvail, Y. Molard, Deep red luminescent hybrid copolymer materials with high transition metal cluster content, J. Mater. Chem. C 2 (2014) 1545–1552, https://doi.org/10.1039/c3tc31309c.
[76] F. Tanaka, T. Furuta, M. Okamoto, S. Hirayama, Inverse correlation between efficiency of singlet oxygen production and rate constant for oxygen quenching in the S1 state of anthracene derivatives, Phys. Chem. Chem. Phys. (2004) 1219–1226, https://doi.org/10.1039/b312398g.
[77] É. Pérez-Esteve, M. Ruiz-Rico, C. De La Torre, L.A. Villaescusa, F. Sancenón, M. D. Marcos, P. Amorós, R. Martínez-Máñez, J.M. Barat, Encapsulation of folic acid in different silica porous supports: a comparative study, Food Chem. 196 (2016) 66–75, https://doi.org/10.1016/j.foodchem.2015.09.017.
[78] A. Llopis-Lorente, B. Lozano-Torres, A. Bernardos, R. Martínez-Máñez, F. Sancenón, Mesoporous silica materials for controlled delivery based on enzymes, J. Mater. Chem. B 5 (2017) 3069–3083, https://doi.org/10.1039/c7tb00348j.
[79] B. Lozano-Torres, J.F. Blandez, I. Galiana, A. García-Fernández, M. Alfonso, M. D. Marcos, M. Orzáez, F. Sancenón, R. Martínez-Máñez, Real-time in vivo detection of cellular senescence through the controlled release of the NIR fluorescent dye Nile blue, Angew. Chem. Int. Ed. 59 (2020) 15152–15156, https://doi.org/10.1002/anie.202004142.
[80] F. Grasset, Y. Molard, S. Cordier, F. Dorson, M. Mortier, C. Perrin, M. Guilloux-Viry, T. Sasaki, H. Haneda, When “metal atom clusters” meet ZnO nanocrystals: a ((n-C 4H9)4N)2Mo6Br 14@ZnO hybrid, Adv. Mater. 20 (2008) 1710–1715, https://doi.org/10.1002/adma.200701845.
[81] F. Grasset, F. Dorson, S. Cordier, Y. Molard, C. Perrin, A. Marie, T. Sasaki, H. Haneda, Y. Bando, M. Mortier, Water-in-oil microemulsion preparation and characterization of Cs 2[Mo6X14]@SiO2 phosphor nanoparticles based on transition metal clusters (X = Cl, Br, and I), Adv. Mater. 20 (2008) 143–148, https://doi.org/10.1002/adma.200701686.
[82] K. Kirakci, P. Kubát, M. Dušek, K. Fejfarová, V. Šícha, J. Mosinger, K. Lang, A highly luminescent hexanuclear molybdenum cluster - a promising candidate toward photoactive materials, Eur. J. Inorg. Chem. 8 (2012) 3107–3111, https://doi.org/10.1002/ejic.201200402.
[83] Y.A. Vorotnikov, O.A. Efremova, N.A. Vorotnikova, K.A. Brylev, M.V. Edeleva, A. R. Tsygankova, A.I. Smolentsev, N. Kitamura, Y.V. Mironov, M.A. Shestopalov, On the synthesis and characterisation of luminescent hybrid particles: Mo6 metal cluster complex/SiO2, RSC Adv. 6 (2016) 43367–43375, https://doi.org/10.1039/c6ra04321f.
[84] Y. Yuan, C.J. Zhang, S. Xu, B. Liu, A self-reporting AIE probe with a built-in singlet oxygen sensor for targeted photodynamic ablation of cancer cells, Chem. Sci. 7 (2016) 1862–1866, https://doi.org/10.1039/c5sc03583j.
[85] N. Brandhonneur, Y. Boucaud, A. Verger, N. Dumait, Y. Molard, S. Cordier, G. Dollo, Molybdenum cluster loaded PLGA nanoparticles as efficient tools against epithelial ovarian cancer, Int. J. Pharm. (2020), 120079, https://doi.org/10.1016/j.ijpharm.2020.120079.
[86] K. Kirakci, J. Zelenka, I. Křížová, T. Ruml, K. Lang, Octahedral molybdenum cluster complexes with optimized properties for photodynamic applications, Inorg. Chem. 59 (2020) 9287–9293, https://doi.org/10.1021/acs.inorgchem.0c01173.